Electromagnetic excitation of ^{11}Li

D. Sackett,* K. Ieki,† A. Galonsky, C. A. Bertulani,‡ H. Esbensen,§ J. J. Kruse, W. G. Lynch, D. J. Morrissey, N. A. Orr,‖ B. M. Sherrill, H. Schulz, A. Sustich,¶ and J. A. Winger

National Superconducting Cyclotron Laboratory and Department of Physics and Astronomy, Michigan State University, East Lansing, Michigan 48824

F. Deák, Á. Horváth, and Á. Kiss

Department of Atomic Physics, Eötvös University, Puskin utca 5-7, H-1088 Budapest 8, Hungary

Z. Seres

KFKI Research Institute for Particle and Nuclear Physics of the Hungarian Academy of Sciences, H-1525 Budapest 114, Hungary

J. J. Kolata

Department of Physics, University of Notre Dame, Notre Dame, Indiana 46556

R. E. Warner

Department of Physics, Oberlin College, Oberlin, Ohio 44074

D. L. Humphrey

Department of Physics, Western Kentucky University, Bowling Green, Kentucky 42101

(Received 30 November 1992)

We have performed a kinematically complete measurement of the Coulomb dissociation of 28 MeV/nucleon ^{11}Li into ^{9}Li and two neutrons by a Pb target. From the energies and angles of the emitted neutrons and of ^{9}Li, the excitation energy E of ^{11}Li was determined on an event-by-event basis, and the Coulomb dissociation cross section as a function of excitation energy was constructed. The photonuclear cross section $\sigma_{E1}(E)$ and the dipole strength function $dB(E1)/dE$ were determined from the Coulomb dissociation cross section. $\sigma_{E1}(E)$ has a peak at $E = 1.0$ MeV and a width $\Gamma = 0.8$ MeV. These parameters are consistent with the picture of a soft dipole mode. However, a significant post-breakup Coulomb acceleration of ^{9}Li suggests instead a direct breakup. The complete kinematical measurement also allowed neutron and ^{9}Li momentum distributions to be constructed in the rest frame of the ^{11}Li. The momentum distributions were fitted with Gaussian functions, yielding width parameters $\sigma_9 = 18 \pm 4$ MeV/c and $\sigma_n = 13 \pm 3$ MeV/c. A more general feature of the breakup mechanism of ^{11}Li could be deduced from these measurements. It was found that the ^{9}Li and neutron momentum distributions and the neutron-neutron relative momentum distribution could be reproduced if the ^{11}Li excitation energy was partitioned between the ^{9}Li and the neutrons by a three-body phase space distribution. This indicates there is no directional correlation between the halo neutrons, and shows that the halo neutrons do not exist as a dineutron bound to a ^{9}Li core.

PACS number(s): 25.70.De, 21.10.Gv, 25.20.Dc, 25.60.+v

I. INTRODUCTION

The increasing availability of radioactive nuclear beams has led to the discovery of several unique properties of light, neutron-rich nuclei. The ^{11}Li nucleus, with three protons and eight neutrons has probably received the most attention, both theoretically and experimentally, due to its rather unique structure. In the first experiments to use a ^{11}Li beam, Tanihata *et al.* [1] measured the total interaction cross section for ^{11}Li and determined the matter radius from the interaction cross section. They also determined the interaction cross sections and matter radii for ^{6}Li, ^{7}Li, ^{8}Li, and ^{9}Li and found that ^{11}Li has a larger matter radius than would be expected from the systematics of the matter radii of the

*Present address: NITON Corp, 74 Loomis, Bedford, MA 01730.

†On leave from Department of Physics, Rikkyo University, 3 Nishi-Ikebukuro, Toshima, Tokyo 171, Japan.

‡On leave from Instituto de Física, Universidade Federal do Rio de Janeiro, 21945 Rio de Janeiro, Brazil.

§Permanent address: Physics Division, Argonne National Laboratory, Argonne, IL 60439.

‖Present address: LPC-ISMRA, Bldv. de Marechal Juin, Caen, France.

¶Present address: Department of Computer Science, Mathematics and Physics, Arkansas State University, P.O. Box 70, State University, AR 72467-0070.

less neutron-rich lithium isotopes. This large matter radius implies a long tail in the ^{11}Li density distribution. In a subsequent experiment, Kobayashi *et al.* [2] found that the transverse momentum distribution of ^{9}Li from the fragmentation of ^{11}Li nuclei has a much narrower width than that expected from the Goldhaber model [3] of projectile fragmentation. The narrow width was interpreted to mean that the density distribution of ^{11}Li has a large spatial extent and the two valence neutrons form a neutron halo around the ^{11}Li nucleus [2, 4, 5]. This halo structure arises from the long tail of the wave function of the valence neutrons due to their small binding energy ($S_{2n} = 0.34$ MeV [6]). Hence, the halo is expected to be a common feature of nuclei along the neutron drip line.

It was also found that the two-neutron removal cross section of ^{11}Li increased with the atomic number of the target and became extremely large for high-Z targets such as Pb. To explain the target charge dependence, it was suggested that the Coulomb excitation cross section for ^{11}Li is large. Thus a high-Z target would act as a source of photons that bombard the ^{11}Li projectile as it passes [7]. Since ^{11}Li has no bound excited states, ^{10}Li is unbound to neutron decay, and ^{9}Li is particle stable up to 4.06 MeV [8], Coulomb excitation of ^{11}Li up to 4.4 MeV leads only to Coulomb dissociation into a ^{9}Li and two neutrons. To explain the large Coulomb dissociation cross section, a new type of collective excitation was proposed [4, 9, 10]. In this excitation mode, called a soft dipole resonance (SDR), the ^{9}Li core oscillates against the halo neutrons in the ^{11}Li nucleus. This resonance is therefore mechanically different from the giant dipole resonance (GDR), where all the neutrons oscillate against all the protons. For the SDR, the restoring force of the oscillation is weak because of the low density of the halo. Hence the excitation energy of the resonance is expected to be low, near 1 MeV [4, 10], in contrast to the GDR, where the excitation energy would be about 23 MeV [11]. There have been several theoretical studies of the excitation of the SDR [4, 12–15], but little experimental work has been reported so far because it is necessary to measure the angle and energy of the ^{9}Li and of both neutrons in order to deduce the excitation energy and shape of the SDR. The complete kinematical measurement also allows us to investigate the correlations between the two neutrons. Because ^{10}Li is unbound, the pairing interaction between the two halo neutrons must be crucial to the formation of a bound ^{11}Li system and should play a key role in the halo structure. It has been suggested that the interaction between the halo neutrons may be strong enough to form a dineutron, and that the ^{11}Li structure may consist of a dineutron bound to a ^{9}Li core [4]. The goals of this work were to use the information from a complete kinematical measurement to search for the soft dipole resonance and to better understand the interaction between the halo neutrons as well as their interaction with the ^{9}Li core. We have made such a measurement of the Coulomb dissociation of ^{11}Li by Pb at an incident energy of 28 MeV/nucleon and have presented some of the results in a recent article [16]. This work provides more details of the experiment as well as additional data and interpretation.

We present a brief review of the formalism of Coulomb excitation theory followed by a detailed description of the experiment. Next we present some results from the ^{9}Li singles data and the one-neutron–^{9}Li coincidence ($1n$-^{9}Li) data. Finally, we proceed to the main focus of this work and present several results from the two-neutron–^{9}Li coincidence ($2n$-^{9}Li) events.

The cross section $d^2\sigma/dE\,d\Omega$ for electromagnetic excitation of a projectile in the Coulomb field of a target was derived in first-order perturbation theory by Alder and Winther [17]. We specialize to electric dipole excitation, $\lambda = 1$, and following Ref. [18] find

$$\frac{d^2\sigma_c}{dE\,d\Omega} = \frac{dN_{E1}(E,\Omega)}{d\Omega}\,\frac{\sigma_{E1}(E)}{E}. \tag{1}$$

Here, E is the excitation energy delivered to the projectile and $d\Omega$ is the element of solid angle into which the projectile deflects. The photonuclear cross section $\sigma_{E1}(E)$ is related to the dipole strength function $dB(E1)/dE$ by

$$\sigma_{E1}(E) = \frac{16\pi^3}{9\hbar c}\,E\,\frac{dB(E1)}{dE}. \tag{2}$$

The quantity $dN_{E1}(E,\Omega)/d\Omega$ is given by [18]

$$\frac{dN_{E1}(E,\Omega)}{d\Omega} = \frac{Z_T^2\alpha}{4\pi^2}\left(\frac{c}{v}\right)^2 \varepsilon^4\xi^2 e^{-\pi\xi} \times\left(\frac{\varepsilon^2-1}{\varepsilon^2}\,[K_{i\xi}(\varepsilon\xi)]^2 + [K'_{i\xi}(\varepsilon\xi)]^2\right). \tag{3}$$

Here, Z_T is the target charge, α is the fine structure constant, v is the relative velocity, $\xi = Ea/\hbar\gamma v$, a is half the distance of closest approach for a head-on collision in a strictly Coulomb potential, and $\gamma = 1/\sqrt{1-v^2/c^2}$. The angular dependence in Eq. (3) is given in terms of ε, the eccentricity of the Coulomb orbit, which is related to the Rutherford scattering angle θ of the projectile by $\varepsilon = 1/\sin(\theta/2)$. The function $K_{i\xi}(\varepsilon\xi)$ is a modified Bessel function of imaginary order, and $K'_{i\xi}(\varepsilon)$ is the derivative of K with respect to the argument. Equation (1) can be integrated over all pure Coulomb orbits to yield the cross section as a function of the excitation energy:

$$\frac{d\sigma_c}{dE} = \frac{N_{E1}(E)}{E}\,\sigma_{E1}(E). \tag{4}$$

$N_{E1}(E)$, referred to as the equivalent photon spectrum, is a dimensionless function of the projectile energy and the excitation energy E. $N_{E1}(E)$ represents the number of virtual photons at energy E available to the projectile from the Coulomb field of the target. The quantity $\sigma_{E1}(E)$ reflects the probability that the nucleus will absorb an $E1$ photon of energy E. Thus, the cross section for $E1$ excitation to energy E is a product of the number of $E1$ photons available at an energy E multiplied by the nuclear strength for absorbing such a photon. This formulation of the Coulomb excitation cross section is known as the equivalent photon method [18]. It has a long history of success in predicting the excitation of low-lying collective states in stable projectiles [17], so it

is natural to extend the method to a search for low-lying $E1$ states in neutron-rich nuclei such as ^{11}Li. One of the appealing features of the method is that the measurable quantity in the laboratory, $d\sigma_c/dE$, is related in a straightforward manner to the quantities of theoretical interest, $\sigma_{E1}(E)$ and $dB(E1)/dE$, by the photon spectrum. Thus a measurement of $d\sigma_c/dE$ and a calculation of $N_{E1}(E)$ will yield $\sigma_{E1}(E)$ and $dB(E1)/dE$ directly.

Contributions from other multipole excitations, specifically $M1$ and $E2$, were estimated to be negligible. The expression for $N_{E1}(E)$, valid for all projectile energies, is given in [18]. An approximate expression for relativistic projectile energies is also given in [18]. For a ^{11}Li beam at 28 MeV/nucleon, the relativistic approximation agreed with the exact calculation to within 2%. Both the $M1$ and the $E2$ photon spectra, $N_{M1}(E)$ and $N_{E2}(E)$, were calculated in the relativistic approximation as well [18]. The $M1$ spectrum was several orders of magnitude less than the $E1$ spectrum, but the $E2$ spectrum was about 400 times greater than the $E1$ spectrum in our energy range [18]. However, it has been shown for several models of the ^{11}Li nucleus that $\sigma_{E2}(E) < 10^{-5}\sigma_{E1}(E)$ [19]. Hence, $N_{E2}(E)\sigma_{E2}(E) < 0.004 N_{E1}(E)\sigma_{E1}(E)$.

II. EXPERIMENTAL SETUP

The experimental task was to determine for each dissociation event the energy of the photon absorbed from the field of the Pb nucleus. This was done by measuring the energies and angles of the three decay products of the photoexcited ^{11}Li. A fragment telescope gave the information for the ^{9}Li, and for the neutrons the time-of-flight (TOF) method was used. The detector setup is shown in Fig. 1.

A. The ^{11}Li beam

The energy of the ^{11}Li beam was constrained by two effects, one favoring high energy and the other low energy. High intensity would be best realized if the ^{11}Li, produced by fragmentation of a primary beam, had an energy of about 60 MeV/nucleon, not far below that of the primary beam. On the other hand, the problem of neutron cross talk (Sec. II D) becomes tractable for neutron energies so low that n-p scattering, with its simple two-body kinematics, is the dominant mode of neutron detection in the hydrocarbon scintillator used. The compromise value chosen was 30 MeV/nucleon.

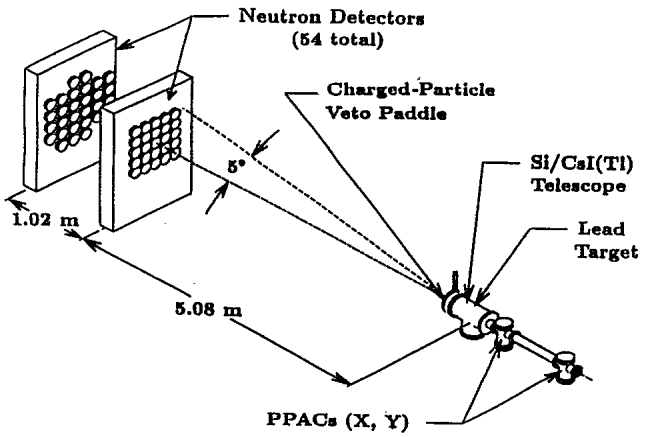

FIG. 1. The detector setup. The detector telescope is located at 0° inside the target chamber, 15 cm downstream from the target. The neutron detectors are mounted in two styrofoam blocks.

A 0.7-g/cm^2 ^{9}Be production target was bombarded with a beam of 80 MeV/nucleon ^{18}O^{6+} produced by the K1200 cyclotron at Michigan State University with an intensity of 1.2×10^{11} particles/s. The ^{11}Li exiting the production target had an average energy of 61 MeV/nucleon. The ^{11}Li was separated from most other reaction products by the A1200 Fragment Separator [20]. It then traversed two dipole magnets and several quadrupole magnets and was degraded to 30 MeV/nucleon before reaching a 0.60-g/cm^2 Pb target in the experimental vault. The degrader was a 7-cm-thick plastic scintillator (called $S1$) with a phototube placed after the first dipole magnet. The dipole magnet produced a dispersion in the beam, hence $S1$ was machined into a wedgelike shape to match the predicted dispersion, thereby minimizing the energy spread induced in the ^{11}Li beam by $S1$. After $S1$, the beam traversed the second dipole (a 14° bend) and entered the experimental area. The experimental area was shielded from the beamline containing $S1$ by a concrete wall 1.4 m thick. Because of the 14° bend in the beamline and the concrete wall, few neutrons produced by reactions in S1 reached our neutron detector array. The TOF of each beam particle was measured across a 15.45-m flight path between $S1$ and the first ΔE detector in the fragment telescope (described in the next section). The spread of the beam was $\pm$2.5 MeV/nucleon. Energy loss in the target was 4.0 MeV/nucleon. The average energy of ^{9}Li from ^{11}Li dissociation in the Pb target was 28 MeV/nucleon, for a total of 252 MeV. An average of 400 ^{11}Li/s reached the Pb target, and the beam was approximately 80% ^{11}Li. The major contaminants, 12% ^{8}He at 25 MeV/nucleon and 6% tritons at 45 MeV/nucleon had insufficient total energy to produce events in the energy range of interest here.

The beam spot size at the Pb target was large, about 2.5 cm × 2.5 cm, and the average angular spread of the incident beam was 0.5°. It was necessary to measure the incident angle and target position of each ^{11}Li particle in order to accurately determine the angle of the emitted ^{9}Li fragment. This was done with two position-sensitive parallel plate avalanche counters (PPAC's) separated by 1.09 m. With the position information from the PPAC's, the incident angle and target position of the ^{11}Li particle could be calculated. The PPAC's were filled with isooctane gas at a pressure of 5 torr. The signals in the PPAC's were resistively divided into up, down, left, and right signals. From these pulse heights, the particle position in each PPAC was calculated with a resolution of 1.5 mm. The PPAC detection efficiency for ^{11}Li was greater than 99.7%.

B. The fragment detectors

The ^{11}Li and ^{9}Li fragments were detected and identified with a Si/CsI(Tl) telescope centered at 0°. The telescope consisted of two Si ΔE detectors and a CsI(Tl) E detector. The first ΔE detector was a MICRON position-sensitive Si strip detector 5 cm × 5 cm × 300 μm, con-

sisting of 16 horizontal strips on one side and 16 vertical strips on the other [21]. Each strip was 3.125 mm wide. The detector was 14.6 cm from the target and it subtended a half-angle of 9°. The group of 16 horizontal and 16 vertical strips could be thought of as forming a grid consisting of 256 square pixels with sides of length 3.125 mm. The angle of the ^{9}Li was determined by the pixel that the particle traversed and that pixel was identified by the ΔE signals from the horizontal and vertical strips that were struck. A fast signal was also picked off the ΔE pulse coming from the struck horizontal strip. The fast signal provided a stop for the neutron TOF measurement and a start for the incident ^{11}Li TOF measurement. Three of the horizontal strips (nos. 8, 15, and 16) did not work during the experiment. The second ΔE detector, a MICRON 5 cm × 5 cm × 300 μm Si detector, was placed behind the strip detector to increase the ratio of energy loss to straggling.

The remaining energy was measured with a CsI(Tl) crystal 6 cm × 6 cm × 1.2 cm thick, the light being readout with four Hamamatsu S3204 PIN diodes attached to the back of the CsI(Tl) crystal. The CsI(Tl) was calibrated with ^{9}Li beams of energies 34.0 and 45.0 MeV/nucleon. The calibration beams were also produced by the fragmentation of ^{18}O on a ^{9}Be target and separated by the A1200 Fragment Separator. Although the light output from CsI(Tl) is not generally proportional to the deposited energy, for high-energy particles over a limited energy range, the response is quite linear [22]. Therefore two calibration points for ^{9}Li were sufficient. The ^{9}Li energy spread was limited to 0.6% full width at half maximum (FWHM) and the absolute value of the energy centroid was determined to 0.2%. Both $S1$ and the Pb target were removed during the calibration.

One disadvantage of CsI(Tl) crystals is that their light output may depend upon where the particle strikes the crystal due to nonuniformity of the thallium doping [23]. Using the grid defined by the Si strip detector, the CsI(Tl) crystal could also be considered a grid of 256 square pixels. For each calibration beam, the light output from each pixel was determined separately. The light output varied by as much as 25% over the area of the crystal. Therefore, a separate calibration was made for each pixel region. Using this technique, the energy resolution was about 2% FWHM, or 6 MeV for the lower-energy calibration beam, which was more than adequate. In general, the light output from a CsI(Tl) crystal depends not only on the incident energy, but also on the charge Z and mass number A of the impinging particle [24, 25]. In addition to ^{9}Li, the calibration beam contained small quantities of several other isotopes. Calibration points for ^{7}Li, ^{8}Li, ^{9}Be, ^{10}Be, ^{11}Be, ^{12}Be, ^{11}B, ^{12}B, ^{13}B, ^{14}B, ^{14}C, ^{15}C, and ^{16}C were also available. We repeated the calibration procedure for these particles and found a Z dependence for all the calibrations, but a negligible A dependence.

C. The neutron detectors

The neutrons were detected with an array of 54 cylindrical detectors, each about 7.4 cm thick and 12.5 cm in diameter filled with either Bicron 501 or NE 213 liquid scintillator. As shown in Fig. 1, the detectors were arranged in two layers about 5 and 6 m from the target. There were 25 detectors in the first array and 29 in the second. In each array the detectors were inserted into holes cut in a block of styrofoam 20 cm thick and 1.22 m on a side. Because the dominant reaction channel was expected to be low-energy Coulomb excitation of ^{11}Li followed by decay to a ^{9}Li and two neutrons, the neutrons were expected to be concentrated in the forward direction. Therefore all the detectors were placed at forward angles. The detector arrays were centered at 0° and subtended a half-angle of 5°. The neutron energies were measured via the time-of-flight method using the fast signal from the neutron detector as a start and the fragment signal in ΔE_1 as the stop. The timing resolution was 1.2 ns. A veto paddle was placed just outside the target chamber to reject any charged particles that might reach the neutron detectors.

Gamma rays from fragment–γ-ray coincidence measurements provided the calibration for the neutron TOF measurement. Although the neutrons were predominately in the forward direction, the γ rays were produced much more isotropically, and almost all of them missed the neutron detectors. In order to produce a substantial γ-ray peak in the TOF spectrum of each neutron detector, each detector array was placed 0.5 m from the target instead of the 5 or 6 m used during the rest of the experiment. This increased the solid angle coverage by a factor of 100 and 144 for the array at 5 and 6 m, respectively. To avoid confusion as to the origin of the γ rays, the Pb target was removed during the calibration, leaving the fragment telescope as the only localized source of γ rays. From off-line analysis of the data we learned that many more γ rays were produced in the telescope than in the target. Also, the analysis showed that for some detectors a telescope γ-ray peak was visible in the time spectrum taken at 5 m. The clearest example, for a neutron detector at 1.7°, is given by the peak at 19 ns in Fig. 2(a). Comparison of such low-statistics peaks

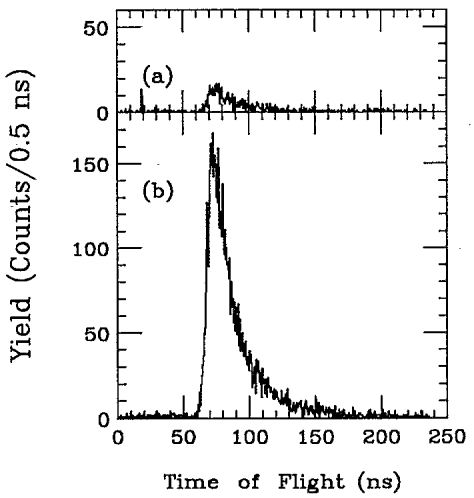

FIG. 2. (a) A time-of-flight spectrum for ^{9}Li–γ-ray coincidence events. (b) A time-of-flight spectrum for ^{9}Li-neutron coincidence events.

with the stronger ones obtained at 0.5 m gives 0.2 ns as a maximum possible systematic error in the neutron flight time.

The γ-ray background was determined via pulse-shape discrimination [26]. The number of γ-ray–^{9}Li coincidences was about 10% of the number of $1n$-^{9}Li coincidences. Except for the peak at 19 ns in Fig. 2(a), the γ-ray and neutron TOF spectra in Fig. 2 are well correlated. We suspect that γ rays with TOF's similar to the neutron TOF's resulted from neutron reactions with the liquid scintillator or surrounding detector material, reactions in which a γ ray was produced and made a pulse in the same detector or in a neighboring detector. We estimated the number of detected γ rays from such neutron reactions. Using the cross sections for γ-ray-producing neutron reactions with the carbon in the scintillator, the carbon, oxygen, and nitrogen in the light pipe, the silicon and oxygen in the glass cell holding the scintillator and the aluminum in the detector housing, and considering the γ-ray efficiency of the neutron detectors, we estimated the number of γ-ray–^{9}Li coincidences to be about 8% of the number of neutron-^{9}Li coincidences. This is in good agreement with the measured value of 10% and supports our hypothesis regarding the source of most of the γ rays.

To measure neutron background from scattering in the target chamber or surrounding areas in the vault, some data were taken with a shadow bar placed just after the target chamber, in place of the veto paddle (Fig. 1) to block neutrons coming directly from the target. This contribution was found to be <2%.

D. Cross talk

The measured triple coincidence events (^{9}Li plus two neutrons) contain a mixture of true neutron-neutron (n-n) events and cross-talk events. Cross talk occurs when one neutron makes a signal in a detector and scatters into another detector, making a signal there too. Cross-talk events are more probable for detectors that are close together because of the large solid angle available to the scattered neutron from the neighboring detectors. Since the cross-talk contribution is not necessarily negligible [27, 28], some care must be taken to identify it and subtract it from the data.

We examined the kinematics of each event and rejected those events that could have been cross talk. The average neutron energy was about 27 MeV. At this energy, the most probable interactions with the detector that yield a neutron that would then be available for cross talk are

$$n + p \rightarrow n + p, \tag{5}$$

$$n + C \rightarrow n + C, \tag{6}$$

$$n + C \rightarrow n + 3\,\alpha\ - 7.6\ \text{MeV}. \tag{7}$$

A neutron detector threshold above 1-MeV electron energy restricts the detected events mostly to those resulting from n-p elastic scattering because the α particles and carbon create only a small amount of light in the scintillator.

For a true coincidence event, the TOF of each neutron and the recoil energies of the protons in the scintillators are measured. For a cross-talk event, the TOF of one neutron, the time required for the same neutron to traverse the distance to the next detector, and the recoil proton energies are determined. An energy spectrum, defined as counts per MeV versus ΔE_n, where $\Delta E_n = E_n - E_s - E_p$, was made from all the triple coincidence events. For the cross-talk events, E_n is the energy of a neutron, E_p is the energy of the recoil proton scattered by this neutron, and E_s is the energy of this neutron after it has scattered from the proton in the scintillator. For the cross-talk events, ΔE_n should be zero by energy conservation, but for true coincidences, ΔE_n is completely random since the energy E_s is then a meaningless quantity. Therefore, when the geometry for n-p scattering is well defined, a ΔE_n spectrum will consist of a peak at $\Delta E_n = 0$ from the cross-talk events and a broad distribution from the true coincidences.

A gate was drawn around the peak at $\Delta E_n = 0$ and events within this gate were rejected as cross talk. In a separate experiment the ^{7}Li(p, n) reaction was used to generate neutrons at 27 MeV and send them into a neutron detector array of similar geometry. In this case, all n-n coincidence events were cross talk, so the ΔE_n spectrum consisted mainly of a peak around $\Delta E_n = 0$. The width of the gate required to reject cross talk was taken from this spectrum. Twenty percent of all the events in the ^{11}Li data were rejected by this procedure. The remaining events, called the *true events*, were used in the remainder of this work. Because the true coincidences yielded arbitrary values for ΔE_n, some true coincidence events were within the ΔE_n gate and were therefore erroneously rejected as cross talk. A Monte Carlo study using the cross-section data of Cecil *et al.* [29] revealed that 13% of the events rejected, that is, 2.6% of all the events, could have been true coincidences that were erroneously rejected. The study also showed that the set of *true events* contained at most a 10% contamination by cross-talk events. As a check on the correctness of the Monte Carlo program, we used it with the geometry of the ^{7}Li(p, n) experiment. It gave a ΔE_n spectrum almost the same as determined from the data.

The cross-talk contamination in the *true events* was further studied to determine if any bias was induced in specific spectra. The spectrum of $d\sigma_c/dE$ versus E, which could reveal the shape and peak location of the soft dipole resonance, was constructed in four ways: from all the $2n$-^{9}Li events, from only the *true events*, and from the Monte Carlo simulations with and without cross-talk rejection. The shapes of all four spectra were the same within statistical uncertainties. Therefore, it was concluded that the possible 10% cross-talk contamination present in the *true events* does not affect the shape of the spectrum for $d\sigma_c/dE$.

Another spectrum to test is the n-n relative momentum spectrum. This spectrum might provide insight into the question of a correlation between two halo neutrons. For example, a narrow peak at low relative momentum

would imply a strong correlation or even a dineutron structure for the halo neutrons. However, cross talk between neighboring detectors could also generate a peak at low relative momentum. For detectors which are nearest neighbors, the geometry produces a constraint from two-body (n and p) kinematics that is very broad. Some of the cross-talk events from neighboring detectors could remain in the set of *true events*. The purely cross-talk ^{7}Li(p,n) events, with events in the peak around $\Delta E_n = 0$ deleted, were used to produce an n-n relative momentum spectrum. Relative momentum is defined as $q = |\vec{p}_1 - \vec{p}_2|/2$. This spectrum, shown in Fig. 3, has a sharp peak at 3.5 MeV/c. The n-n relative momentum spectrum for the ^{11}Li breakup is shown in Fig. 4(a). It also has a peak near 3.5 MeV/c. Upon subtraction of the Fig. 3 spectrum, normalized to the number of neutrons in the ^{11}Li experiment, we get the spectrum in Fig. 4(b). The enhancement at 3.5 MeV/c has been eliminated, and the resulting spectrum varies smoothly as a function of the relative momentum.

Another way to correct for cross talk between neighboring detectors is to select only events with large pulse heights in both detectors. This method works because for neighboring detectors the neutron is scattered through a large angle and therefore has a low energy. When this was done for a threshold of 3-MeV electron energy, the n-n relative momentum spectrum had poor statistics but it agreed with the spectrum in Fig. 4(b). The halo neutron correlation will be discussed in a later section (V D), but it can be concluded here that there is no enhancement at low q. It should be noted the same cross-talk correction procedure using the ^{7}Li(p,n) reaction data was used to construct the n-n correlation function presented in a previous article [16].

III. TELESCOPE DATA

Before proceeding to the main focus of this work, the $2n$-^{9}Li events, we present results from the fragment singles measurement in this section and results from the $1n$-^{9}Li measurements in the next section. The telescope counted the total numbers of both ^{9}Li nuclei produced and ^{11}Li nuclei which did not react. In addition, the number of incident ^{11}Li was determined from the beam TOF measurement. From this information, the two-neutron removal cross section σ_{2n} (^{11}Li$\rightarrow$ ^{9}Li + $2n$) and the total reaction cross section $\sigma_{\rm tot}$ for ^{11}Li + Pb at 28 MeV/nucleon were determined. Before presenting the results and comparing to other work, a description of the analysis technique is presented.

A ΔE-E plot for ^{11}Li and ^{9}Li is shown in Fig. 5(a). The distinction between ^{11}Li and ^{9}Li is blurred due to ^{11}Li dissociation that occurs in the CsI. When dissociation occurs in the CsI, the energy signal is a sum of

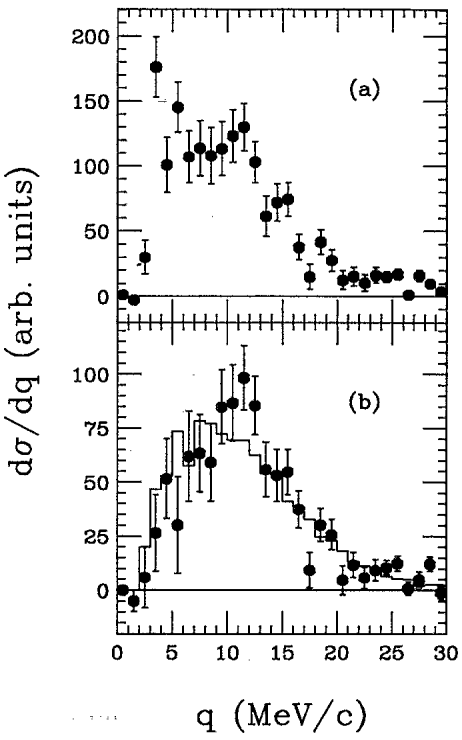

FIG. 4. An n-n relative momentum spectrum from the ^{11}Li data. (a) Before subtracting the cross-talk background measured from the ^{7}Li(p,n) experiment. (b) After subtracting the cross-talk contamination. The histogram is the prediction of a three-body phase space simulation discussed in Sec. V D.

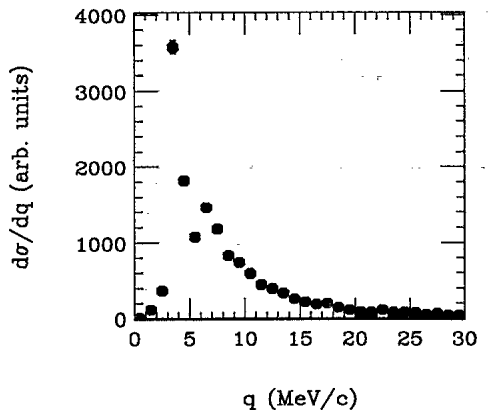

FIG. 3. An n-n relative momentum spectrum due to cross-talk events only, using the ^{7}Li(p,n) reaction to produce neutrons at 27 MeV.

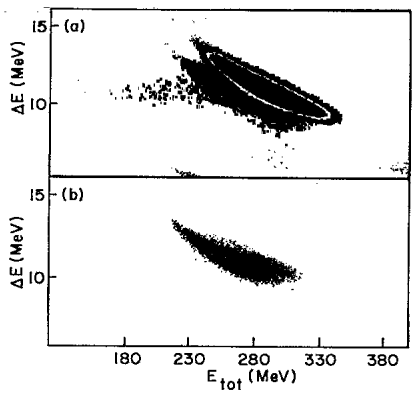

FIG. 5. (a) A two-dimensional ΔE-E plot for the fragment singles events. Only the region around the ^{9}Li and ^{11}Li is shown. (b) A similar plot, but requiring at least one neutron in coincidence with the ^{9}Li fragment.

the ^{11}Li energy loss before dissociation and the ^{9}Li energy after dissociation since the neutrons in general do not deposit any energy. Therefore, the energy signal is greater than that of a ^{9}Li nucleus that enters the CsI, but less than that of a nondissociating ^{11}Li. ^{11}Li may also dissociate in one of the Si ΔE detectors (2×300 μm thick). For these events, the resulting ^{9}Li signal appears in the same location on the ΔE-E plot as ^{9}Li dissociations that occurred in the Pb target. Dissociation in the detector thus makes particle identification ambiguous and generates some ^{9}Li events that appear to come from reactions with the target.

In order to accurately subtract the contribution due to reactions in the telescope, data were also taken with the target removed and the beam energy lowered to compensate for energy loss in the target. The ^{11}Li beam energy was reduced by adding an Al degrader to $S1$. The energy loss of the Al degrader was identical to that of the target, so the ^{11}Li energy striking the detector was the same as in the target-in runs. For any spectrum, a subtraction of target-out data from target-in data yields data representing ^{11}Li reactions in the target. From the ΔE-E spectrum shown in Fig. 5(a), a linearized two-dimensional spectrum of particle identification number (PID) versus $E_{\rm CsI}$ was made using the relation $\mathrm{PID} = E_{\rm tot}^{1.795} - E_{\rm CsI}^{1.795}$. Here, $E_{\rm tot}$ is the sum of the Si and CsI energy signals in MeV and $E_{\rm CsI}$ is the energy deposited in the CsI detector alone. Projecting onto the PID axis, a one-dimensional PID spectrum was made for both target-in and target-out data. These projections are shown in Fig. 6(a). The peak around channel 1000 is from the ^{11}Li beam. The spectrum for the target-out runs has been normalized to the target-in runs for the same number of incident ^{11}Li. Figure 6(b) shows the result of the subtraction of the two spectra in Fig. 6(a). The ^{9}Li peak appears at PID=880, although with a considerable asymmetry. An oversubtraction and an undersubtraction occur for the ^{11}Li data between PID=950 and 1150. It is important to be sure that both the asymmetry in the ^{9}Li peak as well as the oversubtraction and undersubtraction in the ^{11}Li region are not due to a flaw in the subtraction procedure.

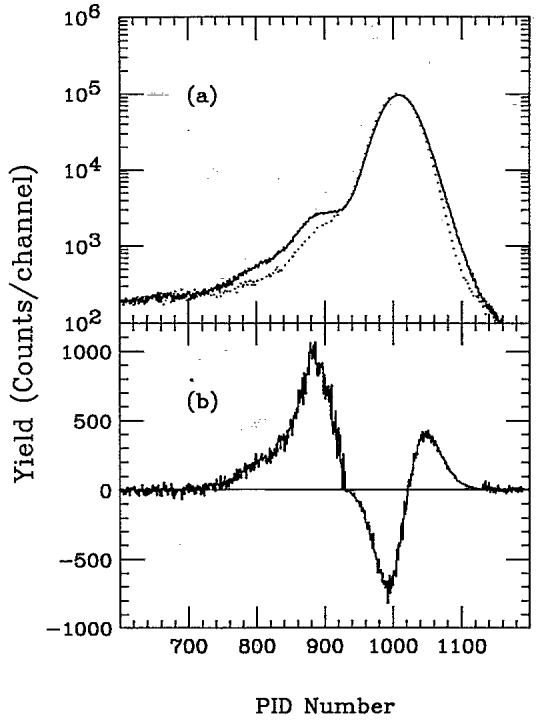

FIG. 6. (a) A one-dimensional particle identification spectrum for target-in data (solid histogram) and target-out data (dotted histogram). (b) The subtracted result. The ^{9}Li peak is near PID=880. The undersubtraction and oversubtraction have been downscaled by a factor of 10 for plotting purposes.

The oversubtraction and undersubtraction between PID=950 and 1150 are most likely caused by differences in the beam energy distributions, although the average beam energies were equal. The energy loss in the Al degrader used in the target-out runs was equal to that in the Pb target, but between the Al degrader and the target there was a final dipole magnet. The rigidity of the ^{11}Li beam for the target-out data was modified by the Al degrader, so a different beam energy distribution was produced at the telescope due to the acceptance of the final dipole magnet. One verification that the subtraction procedure was correct comes from examining the ^{11}Li region shown in Fig. 6(a). The amount of ^{11}Li in the peak region for the target-in data, $N_{11}(\mathrm{in})$, represents the number of ^{11}Li nuclei that are transmitted through the target and telescope without reacting. For the target-out data, the number of ^{11}Li in the peak region, $N_{11}(\mathrm{out})$, represents the number of ^{11}Li nuclei transmitted through the telescope without reacting. Because more flux is removed by the target-plus-telescope than by the telescope only, $N_{11}(\mathrm{in}) < N_{11}(\mathrm{out})$, and the difference $N = N_{11}(\mathrm{in}) - N_{11}(\mathrm{out})$ should be negative. Figure 6(b) shows clearly that N is negative. This is one indication that the subtraction procedure is valid, even though the beam energy distributions for the target-in and target-out data sets were slightly different. The number N was determined by integrating the PID spectrum shown in Fig. 6(b) from PID=930 up to 1200. The result is $N = -118\,000$, and the magnitude of N amounts to 1.7% of the total incident ^{11}Li. The absolute value of N is the amount of incident ^{11}Li removed by the Pb target.

The tail on the ^{9}Li peak was assumed to be caused by reactions between ^{11}Li and Pb other than the two-neutron removal channel. For example, the reaction $^{11}\mathrm{Li} \rightarrow {}^{8}\mathrm{Li} + 3n$ would appear at about PID=790. A more complex reaction yielding an α particle plus ^{6}He, both hitting the CsI(Tl) detector, would appear near PID=850. These reaction products and events from other fragmentation reactions with similar PID values would not be subtracted by the target-out data.

From the subtracted PID spectrum in Fig. 6(b), both the two-neutron removal cross section σ_{2n} and the total interaction cross section $\sigma_{\rm tot}$ for ^{11}Li on Pb can be determined at 28 MeV/nucleon. Fitting the ^{9}Li peak with a Gaussian gives $\sigma_{2n} = 5.1 \pm 0.3$ b. The error arises from extracting a symmetrical peak from the asymmetric peak-plus-tail region. Our measurement can be compared with the result of Anne *et al.* [30]. They found σ_{2n}=5.0±0.8 b for the dissociation of ^{11}Li projectiles on a Au target at 29 MeV/nucleon. They used a Si telescope for particle identification and also performed a

subtraction of target-out data from target-in data. Assuming mostly Coulomb dissociation, their result can be scaled by 1.08 to account for the slight difference in target and beam energy. The 1.08 scaling factor was estimated based on the measured target charge (Z_T) dependence of Coulomb excitation, $Z_T^{1.4}$ [9], and on the inverse beam energy dependence of the Coulomb dissociation cross section [18]. The scaled cross section is σ_{2n}=5.4±0.9 b, in good agreement with our result. The agreement is an indication that the ^{9}Li peak has been correctly extracted from the asymmetric ^{9}Li tail-plus-peak region.

The 1.7% of the incident ^{11}Li beam removed by the Pb target yields a total reaction cross section $\sigma_{\rm tot}$=9.7 ± 0.7 b. The principal source of the uncertainty arises from an error in determining N_{11}(in). The beam TOF measurement that yielded N_{11}(in) required a start signal in the first ΔE detector of the telescope. However, there were some reactions in the Pb target that produced fragments at angles greater that 9°, and these fragments missed the telescope. For events where a fragment did not strike the telescope, the beam TOF could not be determined and, therefore, the incident ^{11}Li particles could not be counted.

Our result for $\sigma_{\rm tot}$ can be compared to the results from Villari *et al.* [31]. They have measured the total reaction cross sections for several neutron-rich nuclei on Si, including ^{11}Li + Si at 25.5 MeV/nucleon and have provided a parametrization of $\sigma_{\rm tot}$ fitted over an energy range of 30–200 MeV/nucleon, a projectile nucleus range of A = 1 to 40, and a target nucleus range of A = 9–209. Using their parametrization yields a total nuclear reaction cross section of 5.7 ± 0.7 b. This cross section represents the total reaction cross section less the Coulomb dissociation cross section, since the parametrization given in Ref. [31] does not include a scaling term for Coulomb excitation. Adding an extracted Coulomb dissociation cross section of 3.8±0.8 b [32] yields a total reaction cross section $\sigma_{\rm tot}$ = 9.5±1.1 b, in good agreement with our result. A somewhat less quantitative comparison can also be made to a result of Blank *et al.* [33], which yielded 7.23 ± 0.78 b for ^{11}Li + Pb at an average ^{11}Li energy of 70 MeV/nucleon. Because the Coulomb dissociation component of $\sigma_{\rm tot}$ is expected to increase by a factor of 70/28 (= 2.5) at our beam energy [18], the two measurements are probably in agreement. Thus it is reasonable to conclude that the target-in and target-out subtraction procedure for the telescope data yields reliable results for both σ_{2n} and $\sigma_{\rm tot}$. Our results for σ_{2n} and $\sigma_{\rm tot}$, as well as cross sections determined from the coincidence measurements, are summarized in Table I.

TABLE I. Compilation of cross sections from the telescope data, the 1n-^{9}Li data, and the 2n-^{9}Li data. The total two-neutron removal cross section is given by σ_{2n} and σ_{1n} is the total neutron cross section from the integrated neutron angular distribution. The cross sections for Coulomb and nuclear dissociation are denoted by σ_c and $\sigma_{\rm nuc}$, respectively. $B(E1)$ is the total strength and σ_{E1} is the photonuclear cross section, determined from the two-neutron-^{9}Li coincidence data. The quantity $^a\sigma_{\rm nuc}$ was calculated in Ref. [32] and $^b\sigma_c$ was determined from the difference between σ_{2n} and $^a\sigma_{\rm nuc}$.

Data set	Quantity	Value
Telescope data	σ_{2n}	5.1 ± 0.3 b
	$\sigma_{\rm tot}$	9.7 ± 0.7 b
1n-^{9}Li data	σ_{1n}	8.3 ± 0.5 b
	σ_c	3.2 ± 0.6 b
	$\sigma_{\rm nuc}$	1.9 ± 0.7 b
2n-^{9}Li data	σ_c	3.6 ± 0.4 b
	$B(E1)$	1.00 ± 0.11 e^2 fm^2
	Total σ_{E1}	4.1 ± 0.5 mb MeV
	$^a\sigma_{\rm nuc}$	1.2 b
	$^b\sigma_c$	3.9 ± 0.3 b

IV. ONE-NEUTRON–^{9}Li COINCIDENCE RESULTS

In this section we present our measurement of the neutron energy and angular distributions and discuss the results in light of previous measurements of the neutron angular distribution.

The ΔE-E spectrum for fragment-neutron coincidence events is shown in Fig. 5(b). The coincidence requirement eliminated the unreacted ^{11}Li from the spectrum. The events shown are due to ^{11}Li breakup in the target, Si ΔE detectors, and CsI. It is not possible to draw a gate that both eliminates events where dissociation occurred in the detector and preserves events where dissociation occurred in the target. Therefore, all coincidence events were used, and, as with the fragment singles data, a target-in, target-out subtraction was performed.

The neutron energy distributions for target in and target out are shown in Fig. 7(a). The target-out data have been normalized to the target-in data by the total number of incident ^{11}Li nuclei. The lower-energy neutrons were produced by neutrons coming from ^{11}Li projectiles that lost energy in the Si and CsI before dissociating. The result of the subtraction is shown in Fig. 7(b). A surprising feature is that the mean energy of the neutrons, 26.9 ± 0.3 MeV, is lower than both the mean ^{9}Li energy and the incident beam energy, 28.3 ± 0.4 MeV/nucleon and 28.0 ± 0.4 MeV/nucleon, respectively, after correcting for the energy loss in the target. This effect will be discussed in more detail in the section on post-breakup Coulomb acceleration (Sec. V C).

The neutron angular distribution could be constructed for angles between 0.5° and 4.8°. The spectrum was corrected for neutron detector efficiency and for attenuation of neutrons by half the Pb target thickness, the Si-CsI telescope, 3 mm of Al at the back of the target chamber, a 6-mm plastic veto paddle, and several meters of air. The angular distribution is given by the solid points in Fig. 8. The open diamonds in Fig. 8 are data taken from Anne *et al.* [30] for ^{11}Li + Au at 29 MeV/nucleon and scaled to our conditions by a factor of 1.08. In the region of overlap the two sets of data are indistinguishable.

By fitting with two Gaussians, shown by the dotted lines in Fig. 8, we then obtained σ_{1n}=8.3 ± 0.5 b for the

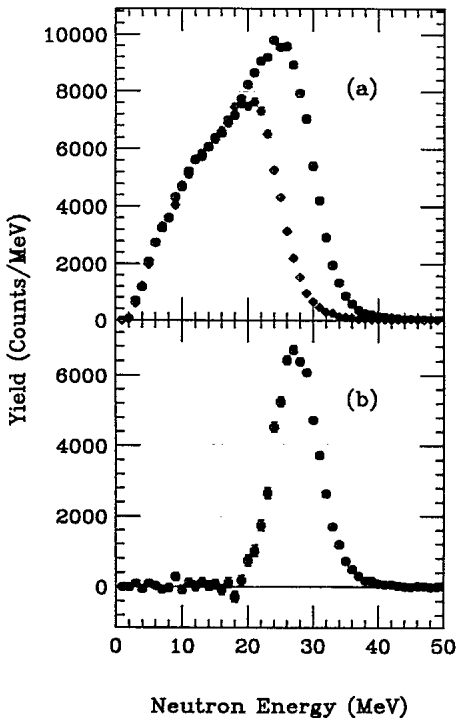

FIG. 7. (a) The neutron energy distributions for target-in (solid points) and target-out (open points). The low-energy portion is due to ^{11}Li dissociation in the CsI. (b) The subtracted result, showing the neutron energy distribution due to the Pb only.

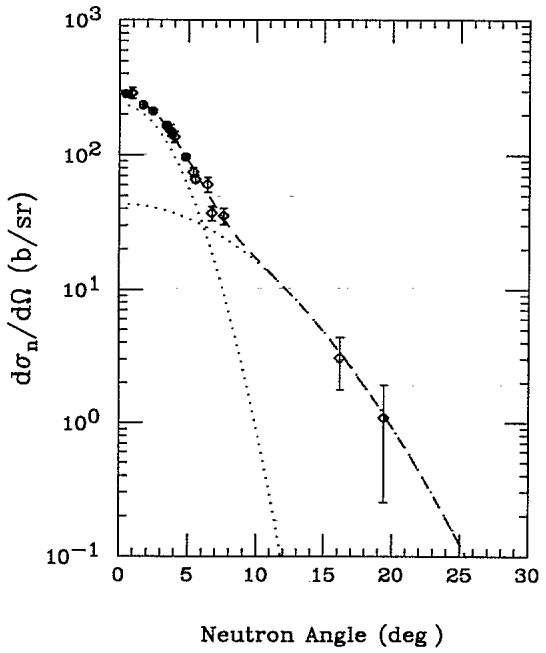

FIG. 8. The measured neutron angular distribution for ^{11}Li + Au at 29 MeV/nucleon taken from [30] (open diamonds). The solid points are for ^{11}Li + Pb at 28 MeV/nucleon (this work). The dotted lines are fits using narrow and broad Gaussians. The dashed line is the sum of both components.

total neutron cross section. The integrated cross section can be interpreted in terms of nuclear and electromagnetic effects and compared to recent calculations of the Coulomb and nuclear dissociation cross sections. Since the equivalent photon spectrum decreases sharply with energy [18], both neutrons, when liberated via Coulomb excitation, will have little excess energy and will tend to be emitted at forward angles in the laboratory. Hence the multiplicity resulting from Coulomb dissociation, m_c, should be $m_c \approx 2$. There will also be nuclear dissociations that produce ^{9}Li and two neutrons where either halo neutron in ^{11}Li may be scattered or absorbed in the Pb target nucleus. The absorption mechanism for the halo neutrons can be thought of in terms of the Serber model [34], where for ^{11}Li a halo neutron may be absorbed by the Pb target nucleus. The projectile remnant, ^{10}Li, is unbound and decays to a ^{9}Li plus a neutron. Because of the low decay energy of ^{10}Li, 150 keV [35] or 800 keV [36], the neutron from ^{10}Li decay would appear at forward angles. Another possibility is the scattering of a halo neutron by the Pb target, also leaving a ^{10}Li fragment. Thus for the combined absorption and scattering mechanisms, if scattering produces a broad angular distribution of neutrons, the nuclear dissociation mechanism would produce both a broad and a narrow neutron angular distribution of neutrons. Because the neutron angular distribution only covers the forward 20°, much of the broad angular distribution would be unobserved. Therefore, the observed neutron multiplicity for nuclear dissociation would be $m_{nuc} \approx 1$.

The Coulomb (σ_c) and nuclear (σ_{nuc}) dissociation cross sections for $^{11}\text{Li} \rightarrow {}^9\text{Li}+2n$ were estimated from the following relations:

$$\sigma_{2n} = \sigma_c + \sigma_{nuc}, \tag{8}$$

$$\sigma_{1n} = m_c\sigma_c + m_{nuc}\sigma_{nuc}. \tag{9}$$

The solution of these equations, with m_c=2 and m_{nuc}=1, yields $\sigma_c = 3.2 \pm 0.6$ b and $\sigma_{nuc} = 1.9 \pm 0.7$ b. These results are listed in Table I. The cross section σ_{nuc} has been calculated for 30 MeV/nucleon ^{11}Li + Au using a diffractive eikonal model [32]. The result, σ_{nuc}=1.2 b, which should increase slightly for a Pb target, agrees with our result 1.9 ± 0.7 b. Subtracting the calculated σ_{nuc}=1.2 b from σ_{2n} yields σ_c=3.9 ±0.3 b, in agreement with $\sigma_c = 3.2 \pm 0.6$ b determined here. Also, a recent calculation for ^{11}Li + Au at 29 MeV/nucleon found that Coulomb dissociation accounts for up to 80% of the total two-neutron removal cross section [37]. The cross sections for σ_c and σ_{nuc} from Eqs. (8) and (9) indicate that 63 ± 16 % of the two-neutron removal cross section is due to Coulomb dissociation, in agreement with the calculation.

V. TWO-NEUTRON–^{9}Li COINCIDENCE RESULTS

To achieve the primary goals of this experiment we used n-n–^{9}Li triple coincidence events to measure the photonuclear excitation function $\sigma_{E1}(E)$ and the dipole

strength function $dB(E1)/dE$. Furthermore, from a reconstruction of these events in the ^{11}Li rest frame, we determined the n-n relative momentum distribution and momentum distributions for single neutrons and for ^{9}Li nuclei. In Sec. V A the technique used to determine the ^{11}Li excitation energy event by event is discussed and in Sec. V B the results for $\sigma_{E1}(E)$ and $dB(E1)/dE$ and comparisons to some calculations are presented. In Sec. V C ^{9}Li and neutron velocity distributions are displayed. The impact of these velocity distributions on the interpretation of the soft dipole resonance will be discussed. Finally, in Sec. V D, ^{9}Li, neutron, and n-n momentum distributions are given. The structure of the ^{11}Li nucleus will be discussed in light of these distributions.

A. The decay energy spectrum

The excitation energy E was determined by measuring the ^{11}Li decay energy, E_d. The excitation energy is related to the decay energy by $E = E_d + S_{2n}$, where S_{2n} is the two-neutron separation energy of ^{11}Li. In the rest frame of the excited ^{11}Li, the decay energy can be expressed as

$$E_d = \frac{1}{2}\mu_1 \vec{V}^2_{2n-9} + \frac{1}{2}\mu_2 \vec{V}^2_{n-n} \qquad (10)$$

with

$$\mu_1 = \frac{m_9(2m_n)}{m_9 + (2m_n)} \text{ and } \mu_2 = \frac{m_n}{2}.$$

Here, $\vec{V}_{2n-9}$ is the relative velocity between the ^{9}Li and the two-neutron center of mass, $\vec{V}_{n-n}$ is the relative velocity between the two neutrons in the rest frame of the two-neutron center of mass, m_9 is the ^{9}Li mass, and m_n is the neutron mass. The relative velocities are measured in the laboratory reference frame and Lorentz transformed to the ^{11}Li rest frame. For our beam energy, the relative velocities are nearly frame invariant, so the Lorentz transform alters the relative velocities <2%. The decay energy was calculated and the decay energy spectrum was constructed from the $2n$-^{9}Li events. Figures 9(a) and (b) display the measured decay energy spectrum for target-in and target-out runs. Approximately 50% of the events are due to dissociation in the Si/CsI telescope. The peak at low decay energies for the target-in data indicates the abundance of events arising from Coulomb dissociation in the Pb target. The subtracted spectrum, representing ^{11}Li decay events in the Pb target, is displayed in Fig. 9(c).

Because both electromagnetic and nuclear interactions may contribute to the decay energy spectrum shown in Fig. 9(c), we must know the nuclear contribution in order to determine the $E1$ strength function. As discussed in Sec. IV, the electromagnetic contribution to the total dissociation cross section may be as high as 80%. We can expect a higher electromagnetic percentage in the present experiment since the geometry selected those dissociation events in which both neutrons were emitted at angles less than 5°.

Nevertheless, an investigation of the contribution from

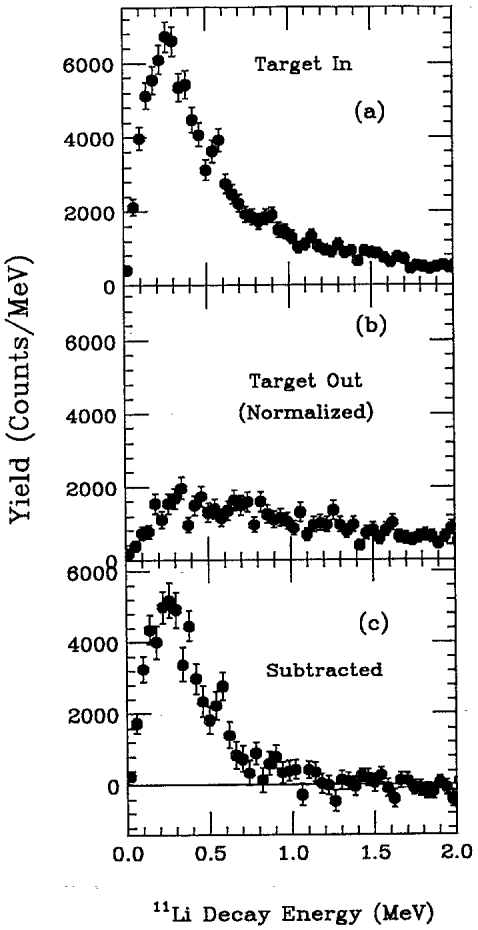

FIG. 9. The decay-energy spectrum for (a) target in, (b) target out, and (c) the subtracted result. The target-out data result from ^{11}Li dissociation in the Si and CsI(Tl) detectors.

nuclear dissociation was performed. Coulomb excitation is largely a peripheral process, occurring at impact parameters $b > b_{\min}$. Here $b_{\min}$ is the impact parameter corresponding to the grazing angle. Using a matter radius of 3.3 fm [1] for ^{11}Li and a Pb radius of 7.1 fm yields $b_{\min} = 10.4$ fm. Nuclear dissociation, where the halo neutrons are scattered or absorbed by the Pb target, occurs for impact parameters $b \leq b_{\min}$. Because of the complete kinematical measurement, an approximate impact parameter could be determined for each event. A decay-energy spectrum was constructed consisting only of events with $b > 15$ fm. In this case the decay energy spectrum is expected to be free of contamination from nuclear dissociations. The impact parameter was determined for each event from the change in the velocity vector of the center of mass before and after breakup since the Coulomb deflection alters the center-of-mass velocity. The center-of-mass velocity after breakup was determined from the measured momenta of the ^{9}Li and the two neutrons. The incident ^{11}Li velocity was measured by TOF and the PPAC's. Recoil of the Pb was neglected in this analysis. The decay energy spectrum, gated on events for b >15 fm, is shown in Fig. 10. The decay energy spectrum for all events (no gating) was shown in Fig. 9(c). Although the magnitude of the gated spectrum is reduced by 25%, the shape of the two spectra agree

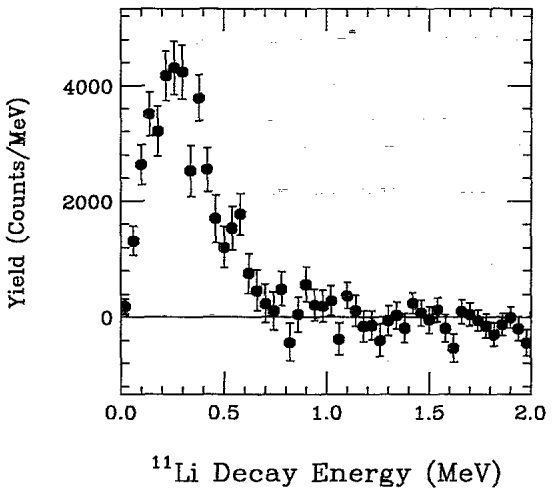

FIG. 10. The decay-energy spectrum gated on impact parameter. Only events with $b > 15$ fm are included here.

within statistical uncertainties. Also, it is not known how many of the events with $b \leq 15$ fm were the result of Coulomb dissociation. Due to the b dependence of the equivalent photon spectrum [18], the Coulomb dissociation increases considerably as b decreases. It is quite possible that many of these events originated from Coulomb dissociation. Therefore, the data from the ungated decay energy spectrum was used, with the knowledge that events from nuclear dissociation were not numerous enough to affect the shape of the spectrum, but that the integrated spectrum might overestimate the number of events from Coulomb dissociation and hence the magnitude of σ_c.

The decay energy spectrum was corrected for the efficiency of the detection system. The efficiency for several decay energies was determined by a Monte Carlo calculation. An empirical fit to the calculated efficiency is shown in Fig. 11. The efficiency is mainly determined

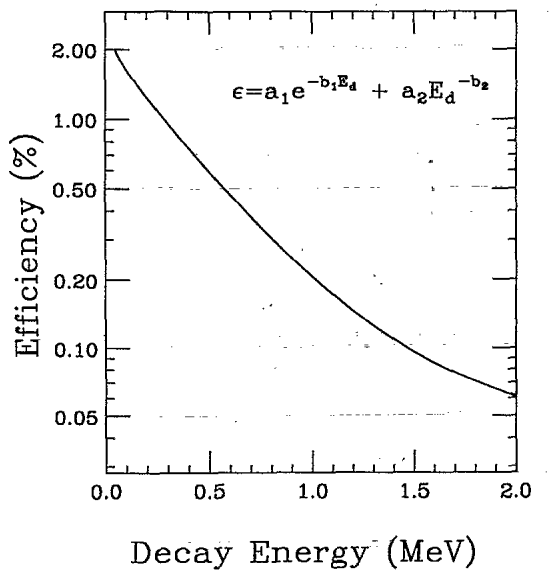

FIG. 11. The detection efficiency as a function of decay energy.

by the product of the geometric efficiency for both neutrons striking scintillator and the intrinsic neutron detector efficiency, which is about 18% for each neutron using a threshold corresponding to 3-MeV neutrons. The geometric efficiency is strongly decay-energy dependent since large decay energies yield neutrons with higher transverse momenta, and these neutrons are more likely to miss the detector array.

Using the calculated efficiency, the ^{11}Li flux, and the target thickness, the absolute Coulomb dissociation cross section was determined from the spectrum in Fig. 9(c). Integrating over energy yielded the total cross section, $\sigma_c = 3.6 \pm 0.4$ b. This value is listed in Table I. The magnitude of σ_c determined here is consistent with σ_c determined from the $1n$-^{9}Li data (σ_c=3.2±0.6 b) and from σ_c determined from the difference $\sigma_c = \sigma_{2n} - \sigma_{\rm nuc} = 3.9 \pm 0.3$ b, where σ_{2n}=5.1±0.3 b was measured with the telescope, and $\sigma_{\rm nuc}$=1.2 b from a calculation [32]. The statistical accuracy of the decay energy spectrum shown in Fig. 9(c) is quite low for $E_d > 0.7$ MeV, and the spectrum is consistent with zero for $E_d > 1$ MeV. However, because σ_c determined from the decay energy spectrum is consistent with the values obtained from the fragment singles and from the $1n$-^{9}Li data, it is unlikely that a significant portion of the decay energy spectrum was not observed due to low statistical accuracy or to a cutoff imposed by the detector apparatus. This will also be important when the strength function and photonuclear cross section are calculated and presented in the next section.

B. σ_{E1}(E) and $dB(E1)/dE$

The measured decay energy spectrum $d\sigma_M/dE_d$, shown in Fig. 9(c), is related to the true spectrum $d\sigma_c/dE_d$ by the following:

$$\frac{d\sigma_M}{dE_d}(E_d) = \int \frac{d\sigma_c}{dE'_d}(E'_d)\, \varepsilon(E'_d, E_d)\, dE'_d. \qquad (11)$$

The function $\varepsilon(E'_d, E_d)$ represents the response of the detector system and dictates how much the true decay energy spectrum is distorted by detector-induced biases. Often, $\varepsilon(E'_d, E_d)$ is a complicated function and unfolding such a response function, equivalent to performing the inverse transform of Eq. (11), is quite difficult. The response function of the detection system was studied as a function of decay energy. Computer-generated events at a specific decay energy were fed through a simulated detector system to determine the resolution response. Neutron detector timing and angular resolutions (1 ns and 0.7°), ^{9}Li energy and angular resolutions (3 MeV and 0.6°), energy losses in the Pb target, and multiple scattering effects in the target were all considered. The results for decay energies of 100 keV, 500 keV, and 1 MeV are shown in Figs. 12(a)–(c), respectively. The width of the response function is shown in Fig. 12(d). Because of the tails in the response functions, FWHM is not an appropriate measure of width. Instead, starting from the centroid, the peak was integrated up to a distance $\pm s$ away from the centroid until the area equaled 76% of the total area of the peak. A width was then defined as $2s$.

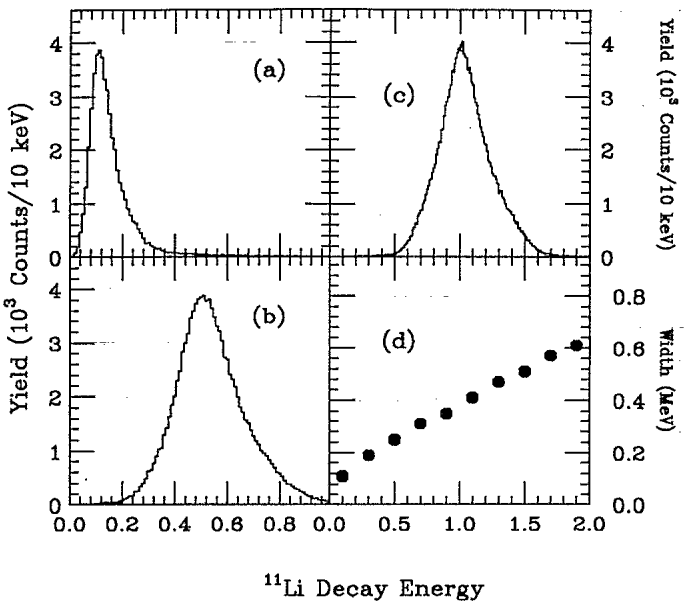

FIG. 12. (a)–(c) The experimental resolution for decay energies of 0.1 MeV, 0.5 MeV, and 1.0 MeV. (d) The width (see text for definition) of the response function vs decay energy.

For a Gaussian distribution $2s$ would be equivalent to FWHM.

Because of the complicated shape of the response function, it was not feasible to unfold $d\sigma_c/dE_d$ from $d\sigma_M/dE_d$ directly. Therefore, model predictions for $d\sigma_c/dE_d$ were chosen, were filtered through a simulated detection system using a Monte Carlo program, and were compared to the measured decay-energy spectrum. The filtering process folds in the effect of the response function $\varepsilon(E'_d, E_d)$ on the true spectrum. A search was performed for a model of the true spectrum that best reproduced the measured decay-energy spectrum. As shown in Eq. (4), $d\sigma_c/dE_d$ is a product of the photon spectrum $N_{E1}(E)$ and a photonuclear cross section. Since the photon spectrum is calculable, constructing a model distribution of $d\sigma_c/dE_d$ only requires a function for $\sigma_{E1}(E)$ to be chosen.

An empirical model, in which $\sigma_{E1}(E)$ was parametrized with a Breit-Wigner function, provided the best reproduction of the data. The Breit-Wigner function is given by

$$\sigma_{E1}(E_d) = \frac{\sigma_m \Gamma}{(E_d - E_0)^2 + (\Gamma/2)^2}, \tag{12}$$

$$\Gamma = \frac{\Gamma(E_0) T(E_d)}{T(E_0)}.$$

The function is written in terms of the decay energy E_d; the excitation energy $E = E_d + S_{2n}$, with S_{2n}=0.34 MeV. The centroid and width are denoted by E_0 and Γ, respectively, and σ_m is a normalization constant. The width includes a transmission coefficient, denoted by $T(E)$, with the energy dependence of s-wave neutrons. The transmission coefficient forces the Breit-Wigner shape to zero at $E_d = 0$. The measured decay energy spectrum, shown in Fig. 9(c), is shown again in Fig. 13(a) after some channel summing was done. The solid line represents the Breit-Wigner model with resonance parameters $E_0 = 0.7$ MeV and $\Gamma = 0.8$ MeV. The good fit of this function after being folded with the response function means that, to within our errors, Eq. (12) represents the experimentally determined photonuclear cross section $\sigma_{E1}(E_d)$. It is shown in Fig. 13(b).

The solid line in Fig. 13(c) gives the dipole strength function $dB(E1)/dE$ determined from σ_{E1}(E) according to Eq. (2). The integrated photonuclear cross section and dipole strength function are 4.1 ± 0.5 mb MeV and 1.00 ± 0.11 e^2 fm^2, respectively. These values are listed in Table I. It is important to emphasize that the solid-line distributions in Figs. 13(b) and (c) were deduced from a decay-energy spectrum free of any dependence on our detection response function and therefore can be

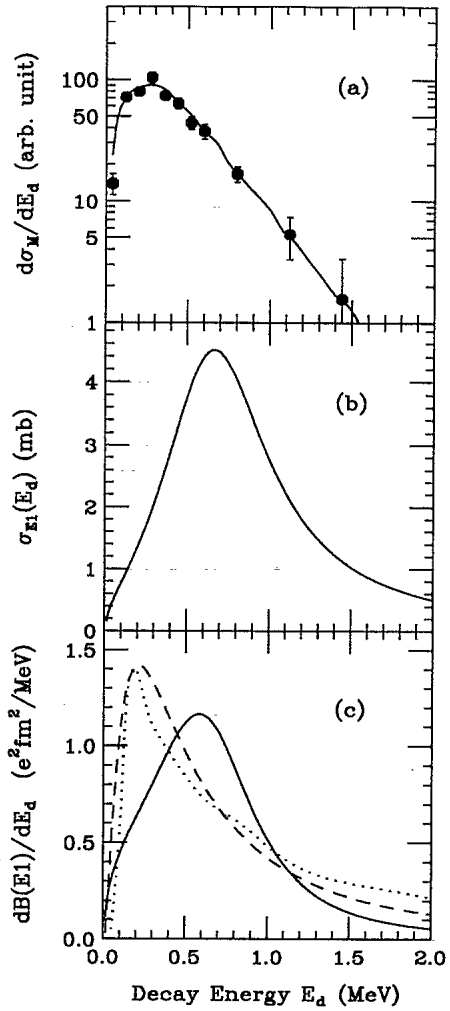

FIG. 13. (a) The decay-energy spectrum. The points are our data and the solid line is the product of a Breit-Wigner function (with $E_0 = 0.7$ MeV and $\Gamma = 0.8$ MeV) and the photon spectrum after being filtered through the detector system. (b) The solid line is the photonuclear cross section corresponding to the Breit-Wigner parameters determined from fitting the data in (a). (c) The solid line is the dipole strength function determined from the data. The dashed line is a calculation using a dineutron-cluster model [15] and the dotted line comes from a correlated-state model [14].

compared directly to theoretical calculations.

The peak in the spectrum for $\sigma_{E1}(E)$ ($E_0 = 0.7$ MeV) is suggestive of a soft dipole resonance for ^{11}Li and is in good agreement with the predictions of several calculations. Broadly speaking, the models of ^{11}Li excitation can be grouped into two categories. The first group assumes a direct breakup into ^{9}Li and two neutrons, while the second group considers the existence of a continuum resonant state in ^{11}Li that can be populated by $E1$ excitation followed by breakup into a ^{9}Li and two neutrons. In the direct breakup picture, the absorbed photon induces a displacement of the ^{9}Li core relative to the halo, and the restoring force provided by the halo is too weak to keep the ^{11}Li nucleus from dissociating into a ^{9}Li and two neutrons. Alternatively, in the resonant-state picture, the restoring force is strong enough such that $E1$ excitation populates a vibrational mode between the ^{9}Li core and the halo. Using a direct breakup scheme, the resonance was originally predicted to exist at a mean decay energy of E_d =0.7 MeV [4]. Another direct breakup calculation, the dineutron-cluster model [15], found the dipole strength function to be peaked near E_d=0.2 MeV. The dipole strength function predicted by this model is shown in Fig. 13(c) by the dashed line. The total strength predicted by the cluster model is $B(E1) = 1.34\ e^2\,\mathrm{fm}^2$, close to the measured value of $1.00 \pm 0.11\ e^2\,\mathrm{fm}^2$, but the model strength function peaks at a considerably lower energy. For the resonant-state picture, a correlated-state model [14] also predicts a peak in the dipole strength function near $E_d = 0.2$ MeV, as shown in Fig. 13(c) by the dotted line. Another model of the resonant state as a vibration between the halo neutrons and the ^{9}Li core predicted peaks at energies of E_d=0.5 and 2.5 MeV [10]. A calculation that modeled the SDR as a collective vibrational mode and was constrained to reproduce the measured Coulomb dissociation cross section found $E_0 = 0.7$ MeV and $\Gamma = 0.7$ MeV [9]. However, we showed in a previous report [16] that the lifetime of a collective state with these parameters would be only 1/5 of an oscillation period. It is difficult to accept the concept of a collective vibrational state with this constraint.

It can be concluded that the photonuclear cross section has a peak near a decay energy of 0.7 MeV with a width of 0.8 MeV, but it is not possible, based solely on these data, to determine whether the breakup occurs directly or passes through a resonant state. The question of the nature of the breakup mechanism will be addressed in the following section.

C. Post-breakup Coulomb acceleration

Some ^{9}Li and neutron velocity distributions provide the means to discriminate between a direct breakup and a resonant-state picture for the excitation of ^{11}Li. Figure 14(a) shows the magnitude of the velocity difference $\Delta V = V_9 - V_{2n}$, where V_9 is the magnitude of the ^{9}Li velocity and V_{2n} is the magnitude of the average neutron velocity for each $2n$-^{9}Li event. The centroid of the distribution appears at $0.0090 \pm 0.0003c$, indicating that the ^{9}Li is, on the average, more energetic than the neutrons.

Before interpreting the velocity difference, it is important to be sure that the result is not produced by detector biases or systematic errors in the energy and angle measurements. The former was investigated via Monte Carlo calculations. Computer-generated events with ΔV distributed about zero were fed through the simulated detector array. The result of the simulation, shown by the histogram in Fig. 14(a) is peaked around zero, indicating that instrumental biases are not causing the shift observed in the data. In Sec. II B the systematic error in fragment energy was given as 0.2%. That translates into 0.000 25 for v_9/c. In Sec. II C we gave evidence that the systematic error in the neutron TOF was less than 0.2 ns. The corresponding error in v_n/c is 0.0007. The uncertainty in $(v_9 - v_{2n})/c$ is less than 0.001, a value that is only 10% of the observed velocity difference.

As an additional check for systematic errors, overall momentum conservation could be verified since the complete kinematics were measured. Figure 14(b) displays the spectrum of counts versus the z component of the center-of-mass velocity after breakup minus the z compo-

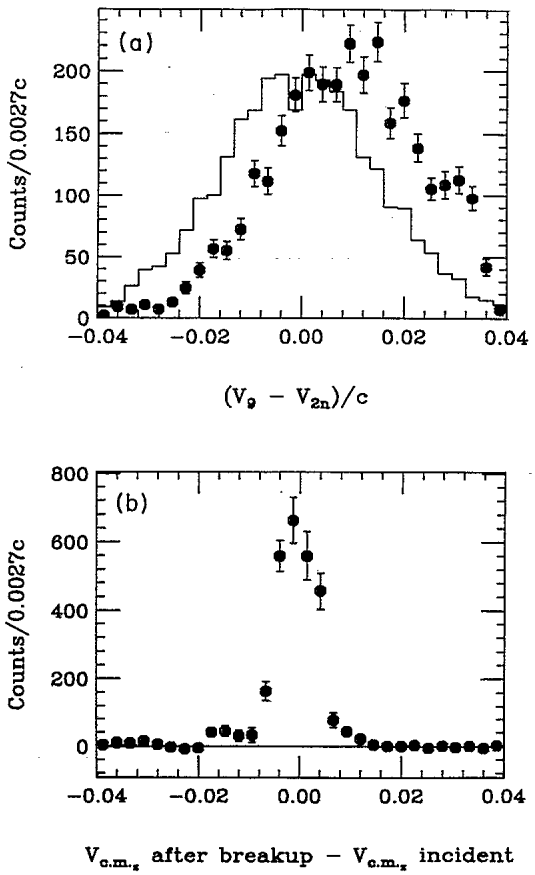

FIG. 14. (a) The spectrum for the velocity difference $V_9 - V_{2n}$, where V_{2n} is the average velocity of the two detected neutrons. The histogram is the result of a simulation using an initial distribution with the velocity difference peaked at zero. (b) The spectrum for the z component of the center-of-mass velocity before breakup subtracted from the center-of-mass velocity after breakup. The near-zero centroid reflects overall momentum conservation. The width of the peak, about 0.008c FWHM, represents the overall velocity resolution of the system.

nent of the center-of-mass velocity before breakup. After breakup, the center-of-mass velocity is determined from the measured velocities of the ^{9}Li and both neutrons. Before breakup, the center-of-mass velocity is given by the measured energy and direction of the incident ^{11}Li. The z components of velocity were used because the contribution from the Pb nucleus, which recoils close to 90°, was negligible in this case. The near-zero centroid of the distribution, $-0.0010c \pm 0.0001c$, showed momentum conservation is quite well enforced and provided a good check that the shift in the z component of ΔV was not due to systematic error. The width of the distribution in Fig. 14(b) yields the overall velocity resolution of the detection system, $0.008c$ FWHM.

It appears that the difference between the ^{9}Li velocity and the average neutron velocity is a real effect, and it can be interpreted in terms of the breakup mechanism. Coulomb excitation is more likely to occur when the ^{11}Li projectile is close to the Pb nucleus, due to the greater intensity of the photon spectrum [18]. If the breakup occurs soon after excitation, the ^{9}Li will be reaccelerated by the Coulomb field of the Pb nucleus, thus yielding events in which the ^{9}Li velocity is greater than the neutron velocity. Because the breakup is occurring close to the Pb nucleus, either the $E1$ excitation is populating a resonant state with a short lifetime or the breakup is direct.

In the case of a resonant state, the meanlife τ of the resonance can be roughly estimated from the difference in the z components of the ^{9}Li velocity and the average velocity of the two neutrons [38]. The z direction is the direction along the beamline. For the z components of velocity, the centroid of the relative velocity distribution was $0.0080 \pm 0.0003c$. Figure 15 is a schematic view of a ^{11}Li dissociation. A straight line trajectory is assumed, since the ^{11}Li is only deflected by a few degrees. It is also assumed that the excitation occurs at the distance of closest approach because the electric field is the most intense at that point [18]. The beam velocity is denoted by V, and τ is the meanlife of the resonance. The distance from the Pb nucleus to the breakup point is denoted by r. After breakup, the ^{9}Li regains the Coulomb energy $U = Z_{\rm Li}Z_{\rm Pb}\,e^2/r$. The equation of motion for the velocity of ^{9}Li after breakup is

$$\frac{d\vec{V}}{dt} = \frac{Z_{\rm Li}Z_{\rm Pb}e^2}{m_9 r^2}\,\frac{\vec{r}}{r} \qquad (13)$$

and

$$\vec{r} = b\hat{x} + Vt\hat{z}.$$

For the z component, integrating from $t = \tau$ to $t = \infty$ yields the result

$$V_{9z}(\infty) - V_{9z}(\tau) = \frac{Z_{\rm Li}Z_{\rm Pb}e^2}{m_9 V}\,\frac{1}{\sqrt{b^2 + V^2\tau^2}}. \qquad (14)$$

The velocity $V_{9z}(\infty)$ is calculated from the measured ^{9}Li energy. The velocity $V_{9z}(\tau)$ at the point of ^{11}Li breakup

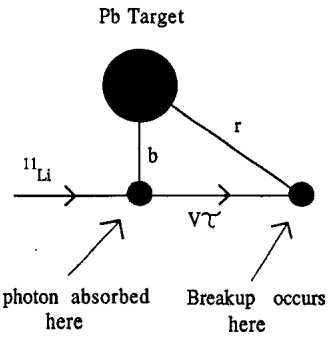

FIG. 15. A schematic view of a ^{11}Li breakup. The average impact parameter is $b = 20$ fm. The distance from the Pb nucleus to the breakup point is denoted by r. V is the beam velocity and τ is the meanlife of the resonance.

is unknown, but because the decay energy is only about 0.6 MeV, it can be assumed to be equal to the average neutron velocity $V_{2nz}(\tau)$ at that point. Because the neutron velocities are not affected by the Coulomb force, $V_{2nz}(\tau) = V_{2nz}(\infty)$, where $V_{2nz}(\infty)$ is the average neutron velocity determined from the TOF measurements of the two emitted neutrons. Therefore, $V_{9z}(\tau) = V_{2nz}(\infty)$, and the centroid of the relative velocity spectrum shown in Fig. 14(a), and given by $\langle \Delta V \rangle = \langle V_{9z}(\infty) - V_{2nz}(\infty) \rangle$, is related to the meanlife of the resonant state as

$$\langle \Delta V \rangle = \frac{Z_{\rm Li}Z_{\rm Pb}e^2}{m_9 V}\,\frac{1}{\sqrt{b^2 + V^2\tau^2}}. \qquad (15)$$

Using an average impact parameter $b = 20$ fm [39] and the centroid of the relative velocity distribution, $\langle \Delta V \rangle = 0.0080 \pm 0.0003c$, the meanlife of a resonant state is $\tau = 50 \pm 7$ fm/c. This meanlife yields a width $\Gamma = 4.0 \pm 0.5$ MeV. Therefore, a resonant state would require a width of approximately 4 MeV to be consistent with the measured velocity difference between the neutrons and the ^{9}Li. It must be reemphasized that this is only intended to be a rough estimate of the width. However, the photonuclear cross section yielded a width of only 0.8 MeV, a factor of 5 too low. If the breakup mechanism proceeded via a resonant state, the width of the resonance from the photonuclear cross section would be consistent with the width determined from the ^{9}Li-neutron energy differences. It is this contradiction between the width determined from the photonuclear cross section and the width implied by neutron-^{9}Li velocity differences that argues against a resonant state and indicates that the breakup mechanism is direct.

It should not be surprising that the presence of a peak in either the $E1$ strength function or the photonuclear cross section does not guarantee the existence of a resonant state. A peak was predicted by the dineutron-cluster model [15]. Recent calculations [40] have shown that, in general, loosely bound systems will have a peak in the strength function near threshold, and that the peak appears because of the large spatial extent of the loosely bound nucleons. A more general argument comes from the fact that the photonuclear cross section will be zero at threshold, rise with increasing phase space, and eventually become zero at high excitation because the inte-

grated cross section must be finite, thus producing a peak in the excitation function.

D. Momentum distributions

Much of the study of ^{11}Li has been dedicated to measuring the momentum distributions of the ^{9}Li and neutrons resulting from the breakup of ^{11}Li on both high-Z and low-Z targets [2, 6, 30, 41, 42]. A recent measurement of parallel momentum distributions of ^{9}Li following breakup on a tantalum target yielded $\sigma_9 \sim 17$ MeV/c, and the width deduced from a measurement of a neutron angular distribution in Refs. [30,42] was $\sigma_n \sim 10$ MeV/c. Because a kinematically complete measurement was performed for this work, the ^{9}Li and the neutron momentum distributions could be constructed in the rest frame of the ^{11}Li. The measured ^{9}Li and neutron momentum distributions are shown in Figs. 16(a) and (b). The momentum distributions in the ^{11}Li rest frame were parametrized by a Gaussian function $d^3\sigma/dp^3 \propto \exp(-p^2/2\sigma_i^2)$, with $\sigma_i = \sigma_9$ or σ_n. An integration over solid angle yielded the function (Maxwellian) used for the fitting: $d\sigma/dp = p^2 \exp(-p^2/2\sigma_i^2)$. For the ^{9}Li and neutron momentum distributions, the best fits yielded $\sigma_9 = 18 \pm 4$ MeV/c, in agreement with Ref. [41] and $\sigma_n = 13 \pm 3$ MeV/c, in agreement with Refs. [30, 42]. These width parameters have been corrected for detector acceptances and resolution.

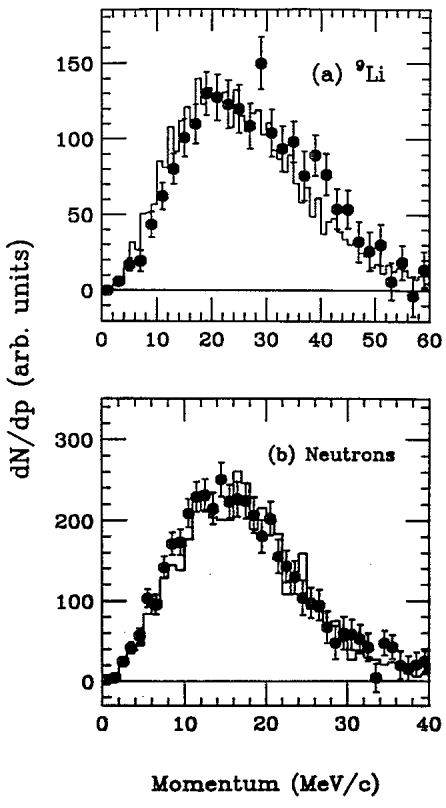

FIG. 16. (a) ^{9}Li momentum distribution determined in the ^{11}Li rest frame. The histogram is the result of a simulation of ^{11}Li breakup with the decay energy partitioned by a three-body phase space distribution. (b) Neutron momentum distribution in the ^{11}Li rest frame. The histogram is the result of the simulation.

The narrow widths of the ^{9}Li and the neutron momentum distributions have been interpreted as evidence for a neutron halo [30, 42] and as an indication of the internal momentum distribution of the ^{11}Li nucleus [41]. The widths of the distributions may also provide some insight into the degree of correlation of the halo neutrons. For example, for no correlation, the width of the neutron momentum distribution is expected to be $\sqrt{2}$ smaller than the width of the ^{9}Li distribution, as suggested by Hansen [43]. Alternatively, if a strong directional correlation exists between the neutrons, then the width $\sigma_n = \sigma_9/2$ since both neutrons recoil against the ^{9}Li.

We offer the interpretation that the widths σ_n and σ_9 may reflect the breakup mechanism of ^{11}Li and the distribution of excitation energy absorbed by the ^{11}Li nucleus. Because of evidence presented earlier that the breakup of ^{11}Li into ^{9}Li and two neutrons following excitation is direct, it is natural to assume the excitation energy is partitioned between the ^{9}Li and the neutrons via a three-body phase space distribution. Therefore, a Monte Carlo simulation of the ^{11}Li breakup was developed that used the product of the measured photonuclear cross section and the equivalent photon spectrum as the input excitation energy distribution. This product represents the ^{11}Li breakup probability as a function of excitation energy. The ^{11}Li decay energy was distributed between the two neutrons and the ^{9}Li based on a three-body phase space distribution, and the angular distributions were chosen to be isotropic in the ^{11}Li rest frame. The simulation also included the detector acceptances. The predictions for the ^{9}Li and neutron momentum distributions are shown by the histograms in Figs. 16(a) and (b), respectively. The good agreement between the histograms and the data supports the interpretation that the ^{9}Li and neutron momentum distributions result from the distribution of excitation energies and the manner in which the excitation energy is partitioned among the three particles.

The three-body phase space formulation also yields information about the degree of correlation between the halo neutrons. The kinetic energy distributions and average kinetic energies for each of the three particles are given by

$$N(T_1)\,dT_1 \propto \sqrt{T_1(T_{1\max} - T_1)}\,dT_1\,, \qquad (16)$$

$$T_{1\max} = \frac{m_2 + m_3}{m_1 + m_2 + m_3}\,E_d,$$

$$\langle T_1 \rangle = \frac{T_{1\max}}{2},$$

and

$$\langle p_1^2 \rangle = m_1 T_{1\max}.$$

The correlation term between the two neutrons can be obtained from momentum conservation:

$$\vec{p}_1 + \vec{p}_2 = -\vec{p}_9, \quad (17)$$

$$\langle \vec{p}_1 \cdot \vec{p}_2 \rangle = \frac{\langle p_9^2 \rangle - \langle p_1^2 \rangle - \langle p_2^2 \rangle}{2}. \quad (18)$$

Here, the subscripts 1 and 2 refer to the neutrons and 9 refers to the ^{9}Li. Substituting in the expressions for the average of the squares of the momenta from (16) yields $\langle \vec{p}_1 \cdot \vec{p}_2 \rangle = -E_d m_n^2 / m_{\rm tot}$ with $m_1 = m_2 = m_n$ now and $m_{\rm tot} = 2m_n + m_9$. The fact that this quantity is negative implies the angle between the neutrons is on the average $> 90^\circ$, hence there is either very little directional correlation, or perhaps an anticorrelation, between the halo neutrons. Using $E_d = 0.7$ MeV, $\langle \vec{p}_1 \cdot \vec{p}_2 \rangle = -59$ MeV$^2/c^2$ and $\langle p_n^2 \rangle = m_n(m_n + m_9)E_d/m_{\rm tot} = 598$ MeV$^2/c^2$. A comparison of these two quantities suggests that θ_{12} is slightly greater than 90°, indicating little directional correlation between the halo neutrons. This result can be compared to a recent calculation of Tanihata *et al.* [44]. In that work $\langle \vec{p}_1 \cdot \vec{p}_2 \rangle$ was calculated as in Eq. (18) above, but using $\langle p_i^2 \rangle = 3\sigma_i^2$ where σ_i is the width of the (Gaussian) momentum distriubutions for ^{9}Li and the neutrons. Using $\sigma_9 = 21 \pm 3$ MeV/c from [2] and $\sigma_n = 10 \pm 1$ MeV/c from [30, 42], they find $\langle \vec{p}_1 \cdot \vec{p}_2 \rangle = 361 \pm 74$ MeV/c. Furthermore, $\langle p_n^2 \rangle = 3\sigma_n^2 = 300 \pm 43$ MeV/c, implying $\theta_{12} = 0^\circ$ and hence a strong directional correlation between the halo neutrons.

Although it is difficult to reconcile these two contradictory results, some additional data, the n-n relative momentum spectrum, can also be shown to agree with the three-body phase space formulation of the ^{11}Li breakup. The n-n relative momentum spectrum was shown in Fig. 4(b). The histogram shown in Fig. 4(b) is a prediction from a Monte Carlo simulation using the three-body phase space assumption. The simulation is in reasonable agreement with the data, although the data are somewhat overpredicted at low relative momenta. It is expected that a strong directional correlation between the halo neutrons, like that predicted in Ref. [44], would produce a peak at low relative momenta, a peak that is not present. Therefore, all of our results, when compared to the predictions of a three-body phase space formulation, suggest that there is no directional correlation between the halo neutrons.

Finally, one caveat regarding this analysis should be mentioned. Our conclusions are based on the success of a three-body phase space formulation in reproducing the measured momentum distributions. It is reasonable to suppose that more sophisticated models that explicitly include correlations between the halo neutrons could also reproduce the measured distributions. For example, a correlated-state model [14] predicts an average opening angle between the neutrons of 92°. It would be desirable to compare the predictions of sophisticated models such as that of Ref. [14] to our data in detail in order to further understand the nature of the interaction between the halo neutrons.

VI. SUMMARY AND CONCLUSIONS

We have measured both fragment singles events and coincidence events from the dissociation of ^{11}Li nuclei at 28 MeV/nucleon on a Pb target. Our results from the fragment singles and $1n$-^{9}Li events are consistent with measurements from several other experiments [6, 33, 30, 42], and we present new results from $2n$-^{9}Li coincident data. From the ^{9}Li fragment singles data, a total two-neutron removal cross section $\sigma_{2n} = 5.1 \pm 0.3$ b was measured. Also, from the number of ^{11}Li nuclei transmitted through the target, a total reaction cross section $\sigma_{\rm tot} = 9.7 \pm 0.7$ b was determined.

The angular distribution for $1n$-^{9}Li events was constructed between 0° and 5°. The angular distribution agreed very well with a previous measurement of the neutron angular distribution for a 29 MeV/nucleon ^{11}Li beam on a Au target [30]. An angle-integrated neutron cross section $\sigma_{1n} = 8.3 \pm 0.5$ b was determined. This cross section could be considered to be a sum of the multiplicity-weighted contributions from Coulomb and nuclear dissociations. For multiplicities m_c=2 and $m_{\rm nuc}$=1 and σ_{2n}=5.1 b, $\sigma_{2n} = \sigma_c + \sigma_{\rm nuc}$, Coulomb and nuclear dissociation cross sections of $\sigma_c = 3.2 \pm 0.6$ b and $\sigma_{\rm nuc} = 1.9 \pm 0.7$ b were calculated. The values of the multiplicities chosen were based on a possible reaction mechanism for nuclear dissociation, namely, absorption of a halo neutron by the Pb nucleus or scattering of it into a broad angular range, and the fact that the angular distribution was limited to a maximum angle of 20°. The results for σ_c and $\sigma_{\rm nuc}$ were in reasonable agreement with two different theoretical estimates of the magnitudes of the Coulomb and nuclear dissociation cross sections [32, 37].

This work focused mainly on the data resulting from the complete kinematical measurement of the $2n$-^{9}Li events. That measurement allowed the ^{11}Li decay energy, and hence the excitation energy, to be determined on an event-by-event basis. From the decay-energy spectrum, an excitation-energy-dependent Coulomb dissociation cross section could be constructed. Dividing out the equivalent photon spectrum then yielded the photonuclear spectrum $\sigma_{E1}(E)$ and the dipole strength function $dB(E1)/dE$. $\sigma_{E1}(E)$ was fitted with a Breit-Wigner resonance shape, yielding a resonance energy of 1.0 MeV and a width $\Gamma = 0.8$ MeV. These parameters are in very good agreement with the location and width of the predicted soft dipole resonance predicted by a variety of models [4, 6, 12, 14, 45]. However, although there is little dispute that a low-energy $E1$ enhancement exists in ^{11}Li due to the large Coulomb dissociation cross section of 3.6 ± 0.4 b, the exact nature of the enhancement is not known. Specifically, there is considerable debate about whether the excited ^{11}Li nucleus breaks up immediately, as in a direct breakup model, or if it populates a collective mode of the type discussed in Refs. [9, 10]. The nature of the enhancement cannot be ascertained merely from the measurement of the photonuclear spectrum.

However, from a shift in a ^{9}Li-neutron relative velocity spectrum, the lifetime of the resonance was estimated to be $\tau = 50$ fm/c, which yields a width $\Gamma = 4$ MeV, greater than the width of the photonuclear cross section by a factor of 5. The contradiction between the width of the photonuclear spectrum and the width implied by the estimated lifetime of the excited ^{11}Li indicates that the

photonuclear cross section does not describe a resonant state; the breakup is direct. Thus our measurement is evidence against the existence of a vibrational excitation mode in ^{11}Li between the halo neutrons and the ^{9}Li core, i.e., against the soft dipole resonance.

Also, from the complete kinematical measurement, ^{9}Li and neutron momentum distributions could be reconstructed in the rest frame of the ^{11}Li nucleus. The distributions were fitted with Gaussian functions and yielded widths $\sigma_9 = 18 \pm 4$ MeV/c and $\sigma_n = 13 \pm 3$ MeV/c, in good agreement with previous measurements [2, 6, 41]. Perhaps the most interesting feature of these momentum distributions was that they could be reproduced by a simulation that used the measured ^{11}Li excitation energy distribution and a three-body phase space distribution to partition that energy amongst the ^{9}Li and the neutrons. This is evidence that there is no directional correlation between the halo neutrons, and the halo neutrons do not exist as a dineutron in the ^{11}Li nucleus.

ACKNOWLEDGMENTS

We thank J. Yurkon and D. Swan for their technical assistance and J. Winfield and R. Fox for their assistance with the data acquisition. We are grateful to G. F. Bertsch and K. Yabana for extensive discussions. Support of the U.S. National Science Foundation under Grant Nos. PHY89-13815, INT86-17683, PHY91-00688, and PHY91-22067 and of the Hungarian Academy of Sciences is gratefully acknowledged.

[1] I. Tanihata, H. Hamagaki, O. Hashimoto, Y. Shida, N. Yoshikawa, K. Sugimoto, O. Yamakawa, T. Kobayashi, and N. Takahashi, Phys. Rev. Lett. **55**, 2676 (1985).
[2] T. Kobayashi, O. Yamakawa, K. Omata, K. Sugimoto, T. Shimoda, N. Takahashi, and I. Tanihata, Phys. Rev. Lett. **60**, 2599 (1988).
[3] A.S. Goldhaber, Phys. Lett. **53B**, 306 (1974).
[4] P. G. Hansen and B. Jonson, Europhys. Lett. **4**, 409 (1987).
[5] R. N. Boyd and I. Tanihata, Phys. Today **45**, 44 (1992).
[6] T. Kobayashi, Nucl. Phys. **A538**, 343c (1992).
[7] G. Baur, C.A. Bertulani, and H. Rebel, Nucl. Phys. **A458**, 188 (1986).
[8] F. Ajzenberg-Selove, Nucl. Phys. **A490**, 1 (1988).
[9] T. Kobayashi, S. Shimoura, I. Tanihata, K. Katori, K. Matsuta, T. Minamisono, K. Sugimoto, W. Muller, D.L. Olson, T.J.M. Symons, and H. Wieman, Phys. Lett. B **232**, 51 (1989).
[10] K. Ikeda, Nucl. Phys. **A538**, 355c (1992).
[11] B.L. Berman and S.C. Fultz, Rev. Mod. Phys. **47**, 713 (1975).
[12] G.F. Bertsch and H. Esbensen, Ann. Phys. **209**, 327 (1991).
[13] N. Teruya, C.A. Bertulani, S. Krewald, H. Dias, and M.S. Hussein, Phys. Rev. C **43**, R2049 (1991).
[14] H. Esbensen and G.F. Bertsch, Nucl. Phys. **A542**, 310 (1992).
[15] C.A. Bertulani, G. Baur, and M.S. Hussein, Nucl. Phys. **A526**, 751 (1991).
[16] K. Ieki, D. Sackett, A. Galonsky, C.A. Bertulani, J.J. Kruse, W.G. Lynch, D.J. Morrissey, N.A. Orr, H. Schultz, B.M. Sherrill, A. Sustich, J.A. Winger, F. Deák, Á. Horváth, Á. Kiss, Z. Seres, J.J. Kolata, R.E. Warner, and D.L. Humphrey, Phys. Rev. Lett. **70**, 730 (1993).
[17] K. Alder and A. Winther, *Electromagnetic Excitation* (North-Holland, Amsterdam, 1975).
[18] C.A. Bertulani and G. Baur, Phys. Rep. **163**, 299 (1988).
[19] C.A. Bertulani and A. Sustich, Phys. Rev. C **46**, 2340 (1992).
[20] B.M. Sherrill, D.J. Morrissey, J.A. Nolen, and J.A. Winger, Nucl. Instrum. Methods B **56/57**, 1106 (1991).
[21] T. Davinson, A.C. Shotter, E.W. Macdonald, S.V. Springham, P. Jobanputra, A.J. Stephens, and S.L. Thomas, Nucl. Instrum. Methods A **288**, 245 (1990).
[22] N. Colonna, G.J. Wozniak, A. Veeck, W. Skulski, G.W. Goth, L. Manduci, P.M. Milazzo, and P.F. Mastinu, Nucl. Instrum. Methods A **321**, 529 (1992).
[23] W.G. Gong, N. Carlin, C.K. Gelbke, and R. Dayton, Nucl. Instrum. Methods A **287**, 639 (1990).
[24] W.G. Gong, Y.D. Kim, G. Poggi, Z. Chen, C.K. Gelbke, W.G. Lynch, M.R. Maier, T. Murakami, M.B. Tsang, and H.M. Xu, Nucl. Instrum. Methods A **268**, 190 (1988).
[25] D. Horn, G.C. Ball, A. Galindo-Uribari, E. Hagberg, and R.B. Walker, Nucl. Instrum. Methods A **320**, 273 (1992).
[26] J. Heltsley, L. Brandon, A. Galonsky, L. Heilbronn, B.A. Remington, S. Langer, A. Vandermolen, and J. Yurkon, Nucl. Instrum. Methods A **263**, 441 (1988).
[27] M. Cronqvist, B. Jonson, T. Nilsson, G. Nyman, K. Riisager, H.A. Roth, O. Skeppstedt, O. Tengblad, K. Wilhelmsen, Nucl. Instrum. Methods A **317**, 273 (1992).
[28] P. Desesquelles, A. Dauchy, A. Giorni, D. Heuer, A. Lleres, C. Morand, J. Saint-Martin, P. Stassi, J.B. Vian, B. Chambon, B. Cheynis, and D. Drain, Nucl. Instrum. Methods A **307**, 366 (1991).
[29] R. A. Cecil, B. D. Anderson, and R. Madey, Nucl. Instrum. Methods **161**, 439 (1979).
[30] R. Anne, S.E. Arnell, R. Bimbot, H. Emling, D. Guillemaud-Mueller, P.G. Hansen, L. Johannsen, B. Jonson, M. Lewitowicz, S. Mattsson, A.C. Mueller, R. Neugart, G. Nyman, F. Pougheon, A. Richter, K. Riisager, M.G. Saint-Laurent, G. Schrieder, O. Sorlin, and K. Wilhelmsen, Phys. Lett. B **250**, 19 (1990).
[31] A.C.C. Villari, W. Mittig, E. Plagnol, Y. Schultz, M. Lewitowicz, L. Bianchi, B. Fernandez, J. Gastebois, A. Gillibert, C. Stephan, L. Tassan-Got, G. Audi, W. Zhan, A. Cunsolo, A. Foti, A. Belezyorov, S. Lukyanov, and Y. Penionzhkevich, Phys. Lett. B **268**, 345 (1991).
[32] A. Sustich, Z. Phys. A **342**, 31 (1992).
[33] B. Blank, J.J. Gaimard, H. Geissel, K.H. Schmidt, H. Stelzer, K. Summerer, D. Bazin, R. Del Moral, J.P. Dufour, A. Fleury, F. Hubert, H.G. Clerc, and M. Steiner, Z. Phys. A **340**, 41 (1991).
[34] R. Serber, Phys. Rev. **72**, 1008 (1947).
[35] A.I. Amelin, M.G. Gornov, Yu. B. Goruv, A.L. Ll'in, P.V. Morokhov, V.A. Pechkurov, V.I. Savel'ev, F.M. Sergeev, S.A. Smirnov, B.A. Chernyshev, R.R. Shafigullin, and A.V. Shishkov, Yad. Fiz. **52**, 1231 (1990) [Sov. J. Nucl.

Phys. **52**, 782 (1990)].
[36] K.H. Wilcox, R.B. Weisenmiller, G.J. Wozniak, N.A. Jelley, D. Ashery, and J. Cerny, Phys. Lett. **59B**, 142 (1975).
[37] R. Shyam, P. Banerjee, and G. Baur, Nucl. Phys. **A540**, 341 (1992).
[38] M.A. Bernstein and W.A. Friedman, Phys. Rev. C **31**, 843 (1985).
[39] G. Baur, *Proceedings of International Symposium on Structure and Reactions of Unstable Nuclei*, Niigata, Japan (World Scientific, Singapore, 1991).
[40] H. Sagawa, N. van Giai, N. Takigawa, and M. Ishihara, private communication.
[41] N.A. Orr, N. Anantaraman, S.M. Austin, C.A. Bertulani, K. Hanold, J.H. Kelley, D.J. Morrissey, B.M. Sherrill, G.A. Souliotis, M. Thoennessen, J.S. Winfield, and J.A. Winger, Phys. Rev. Lett. **69**, 2050 (1992).
[42] K. Riisager, R. Anne, S.E. Arnell, R. Bimbot, H. Emling, D. Guillemaud-Mueller, P.G. Hansen, L. Johannsen, B. Jonson, A. Latimier, M. Lewitowicz, S. Mattsson, A.C. Mueller, R. Neugart, G. Nyman, F. Pougheon, A. Richard, A. Richter, M.G. Saint-Laurent, G. Schrieder, O. Sorlin, and K. Wilhelmsen, Nucl. Phys. **A540**, 365 (1992).
[43] P.G. Hansen, Nature **361**, 501 (1993); Nucl. Phys. A (to be published).
[44] I. Tanihata, T. Kobayashi, T. Suzuki, K. Yoshida, S. Shimoura, K. Sugimoto, K. Matsuta, T. Minamisono, W. Christie, D. Olson, and H. Wieman, Phys. Lett. B **287**, 307 (1992).
[45] C.A. Bertulani and L.F. Canto, Nucl. Phys. **A539**, 163 (1992).